Al-Qadisiyah JournalFor Engineering Sciences 18 (2025) 352 – 359

Contents lists available at: http://qu.edu.iq

Al-Qadisiyah Journal for Engineering Sciences

Journal homepage: https://qjes.qu.edu.iq

Research Paper

Investigation of the structural, morphological, and electrochemical characteristics of $MgFe_2O_4/ZnO$ nanocomposite

Alyaa H. Abdalsalam [1] ✉, ***Noor M. Saadoon*** [1], ***Ali A. Ati*** [2], ***S. Dabagh*** [3,4], ***and A. Salim*** [5]

[1] *Nanotechnology and Advanced Materials Research Center, University of Technology, Baghdad, Iraq.*
[2] *Oil and Gas Engineering Department, University of Technology, Baghdad, Iraq.*
[3] *Institute of Applied Physics "Nello Carrara", National Research Council of Italy (CNR), Sesto Fiorentino, 50019, Italy.*
[4] *Cellular Therapy and Stem Cell Production Application and Research Centre, ESTEM, Eskisehir Osmangazi University, Eskisehir, 26040, Turkey.*
[5] *Laser Center & Physics Department, Faculty of Science, Universiti Teknologi Malaysia, Johor, Malaysia.*

ARTICLE INFO

Article history:
Received 12 May 2025
Received in revised form 02 July 2025
Accepted 23 August 2025

keyword:
Cyclic voltameter
Electron microscopy
Hetero
Nanocomposite
X–ray diffraction
ZnO

ABSTRACT

In the current study, three distinct synthesis techniques the gel, co-precipitation, and solid-state method were employed to synthesize $(MgFe_2O_4)_x/ZnO_{1-x}$ hetero-nanocomposites with varying magnesium ferrite contents (x = 0.03%, 0.06%, and 0.09%). To study the effect of the addition of magnesium ferrite nanoparticles on the structural, morphological, thermal, and electrochemical properties of zinc oxide. X–ray diffraction (XRD), Rietveld refinement technique, Fourier transform infrared (FT-IR) spectroscopy, field-emission scanning electron microscopy (FE-SEM), transmission electron microscopy (TEM), and cyclic voltammetry (CV) were used to investigate the samples. The formation of the spinel cubic structure and hexagonal wurtzite structure of the prepared magnesium ferrite/zinc oxide nanocomposites was confirmed by X-ray diffraction, and no extra phases were detected. The Rietveld-refined X-ray diffraction data revealed spinel cubic and hexagonal wurtzite structures with the P63mc and Fd-3m space group, respectively. The crystallite size decreased from 16 to 15 *nm* upon the substitution of magnesium ferrite nanoparticles, confirming the formation of nano-crystalline$MgFe_2O_4/Zn$O nanocomposites. FT-IR spectra were used to verify the absorption bands of $MgFe_2O_4$, ZnO, and their composites. FE-SEM images revealed the presence of a slight agglomeration of nanoparticles and a non-uniform size distribution. TEM analysis revealed nearly spherical morphologies for all prepared samples, with an average particle size of 19-22 *nm*. There is variation in the crystallite size as estimated from the instruments, which may be due to strain. The electrochemical behavior was investigated using cyclic voltammetry (CV) with a 0.5 M KCl aqueous solution as the electrolyte. The $MgFe_2O_4/ZnO$ nanocomposite exhibited superior rate performance and cycle stability compared to the other samples when their electrochemical performance was analyzed using cyclic voltammetry (CV). According to the physical results, nanocomposite electrodes exhibited enhanced electrochemical performance, high reversibility, and cycle stability, with specific capacitances ranging from 1.87 F/g (0.01 V) to 7.63 F/g (0.002 V), making them promising candidates for pseudocapacitors.

1. Introduction

Semiconductor nanoscale materials have garnered extensive attention in recent years due to their remarkable properties, which are comparable to those of bulk materials, resulting from their small size and surface effects. In particular, semiconductors of transition metal oxide nanoparticles have garnered considerable interest in the scientific and industrial communities due to their potential applications, driven by their unique properties, low cost, non-toxicity, and chemical stability. Zinc oxide (ZnO) is considered one of the most promising binary(metal-oxide) semiconductors, with Numerous applications in microelectronics, transducers, sensors, catalysts, and optoelectronic devices. ZnO nanostructure with controlled size and morphologies including nanorods [1], nanobelts [2], Rings [3], nanotubes [4], tetrapods [5], bowls [6], flowers [7], disks [8], hemispheres [9], can synthesized by using chemical synthesis methods such as hydrothermal synthesis [10], co-precipitation method [11,12], sol-gel [13,14], electrochemical deposition [15], spray pyrolysis [16] chemical vapor deposition [17], and so on, also several physical methods such as radio-frequency magnetron sputtering [18], arc discharge method [19], physical vapor deposition [20], pulsed laser deposition [21,22], and so on. Temperature and pressure are used in hydrothermal processes, which often result in a regulated shape and good crystallinity. Faster and easier, co-precipitation frequently yields smaller nanoparticles; however, occasionally it contains contaminants. Although it takes longer, sol-gel offers excellent uniformity and purity at lower temperatures. Electrochemical deposition works well for precisely controlled thin films. The scalability and advantage of spray pyrolysis in producing porous/hollow structures (good for catalysis)-CVD's remarkable purity and orientation control for cutting-edge electronics. The structural, magnetic, electrical, and catalytic properties of ferrites are significantly influenced by their production method, as variations in particle size result in variations in bandgap energy. This inverse relation between bandgap energy and particle size strongly influences the electric properties, morphology, crystallinity, and cation distribution.

*Corresponding Author.
E-mail address: 11595@uotechnology.edu.iq ; Tel: (+964) 770-888 5624 (Alyaa Abdalsalam)

https://doi.org/10.30772/qjes.2025.160113.1559
2411-7773

Nomenclature

a	Lattice constant, Å	$FE-SEM$	Field Emission Scanning Electron Microscopy
c	Lattice constant, Å	$G.O.F$	Goodness-of-fit
c_s	Specific capacitance (F/g)	hkl	Miller indices
d	Interplan spacing Å	K	Dimensionless shape factor
D	Crystallite size (nm)	M	Metals
D_{XRD}	X-ray diffraction crystallite size (nm)	P	Power density P (kW/kg)
D_{FE-SEM}	Filed emission scan electron microscopy crystallite size (nm)	*Greek Symbols*	
D_{TEM}	Transmission electron microscopy crystallite size (nm)	β	Full width at half maximum (Radius)
E	Energy density (kW/kg)	θ	Bragg angle (Degree)
E	Energy density (kW/kg)	λ	Wavelength (Å)
$FT-IR$	Fourier Transform Infrared Spectroscopy	δ	Inverse spinel

Among these methods, the co-precipitation method is simple, low-cost, has a short duration, is environmentally friendly, provides reasonable control over particle size, and achieves high phase purity. N. Maekawa et al., [22] fabricated ZnO NMs by the ALD technique and reported in the electrolyte of Na_2SO_4 of 65 to 7 F/g, 465 to 8 F/g in 1 M KC1, and 846 to 92 F/g in 6 M KOH. M.G. El-Shaarawy et al.,[23] synthesized ZnO (nanowires, nanorods, and nanospheres) via soft-wet and thermal dry methods. The researchers used standard precipitation with and without CTAB surfactant in the wet method. In the dry method, zinc oxide nano powders were synthesized via the oxidation of zinc metal and through the pyrolysis of zinc carbonate, exhibiting specific capacitance values ranging from 81 to 347 F/g. Xiaoli and his workers prepared zinc oxide nanowires (NWs) and zinc oxide nanocones (NCs) using the hydrothermal growth method and chemically etching of ZnO NWs, respectively, and reported a high specific capacitance of 378.5 F/g in 11 M KOH at a scan rate of 20 mV/s for ZnO NCs [24]. Spinel structure ferrites nanoparticles with the general chemical formula $\left[M_{(1-\delta)}Fe_{\delta}\right]$ $\left[(Fe_{(2-\delta)}M_{\delta}\right]$, where M, and δ are tetrahedral sites (A), octahedral sites [B], divalent cation metal, inversion parameters, respectively, where $\delta = 1$, the structural type is called inverse spinel; if $\delta = 0$, the structural type is called normal spinel; otherwise, if the inversion parameter is between 0 and 1, it is called mixed ferrite. Oxide nanoparticles have diverse practical applications, including photocatalysis [25], fuel cells [26], catalysis [27], ferrofluids, solar cell [28], and coloring pigments, due to their high electrical resistance, moderate magnetization, and chemical stability in both acidic and basic media [29]. $MgFe_2O_4$ is a soft magnetic n-type semiconductor material with partially inverted spinel. The cation distribution has been studied for cubic spinel magnesium ferrite $\left[Mg_{(1-\delta)}Fe_{\delta}\right]_A$ $\left[Fe_{(2-\delta)}Mg_{\delta}\right]_B$ the distribution of metal ions in crystal lattice sites affects the physical and chemical properties of the material. These properties depend significantly on the synthesis method, annealing temperature, shape, and size. $MgFe_2O_4$ has found a wide range of technological applications, including gas sensing [30], humidity sensors [31, 32], and catalysts [33], due to its high electrical resistance, moderate magnetization at room temperature, and high chemical and thermal stability. To enhance the properties of spinel ferrites, magnesium ferrite nanoparticles are synthesized using various methods, including the sol-gel method [34], co-precipitation method [35], gel process [36], and chemical vapor deposition technique [37]. Unchista Wongpratat et al. have investigated the effect of magnesium doping on the structural, optical, electrical, and electrochemical properties of nickel ferrite nanoparticles, which exhibited a higher specific capacitance (259.89 Fg^{-1}) compared to other prepared samples [38]. Furthermore, Zein K. Heiba et al. reported a study on non-stoichiometric magnesium ferrite nanoparticles with an LP30 electrolyte for high-performance anodic materials applications [39]. You Li et al. fabricated magnesium-substituted nickel ferrite using the combustion process and studied their structural, morphological, and electrochemical properties for dye wastewater treatment industries [40]. B. Janani et al. [41] studied the photocatalysis behavior of nanocomposites comprised of $CaFe_2O_4$ magnetic nanoparticles and ZnO nanoparticles prepared via a sonochemical method. The results indicate that the $CaFe_2O_4/ZnO$ nanocomposites exhibit higher antibacterial activity against impact than the individual $CaFe_2O_4$ and ZnO. Sana Munir et al. [42] have reported the fabrication of $NiFe_2O_4/ZnO$ nanocomposites using the ultra-sonication method for environmental and biological applications, which showed good photocatalytic performance for the decolonization of methyl orange, methyl blue, and crystal violet dyes, as well as the nanocomposites exhibited higher antibacterial performance as compared to bare $NiFe_2O_4$ and ZnO. Amira S. Hamed et al. [43] employed solid-state and sol-gel methods to synthesize $ZnO/NiFe_2O_4$ nanocomposites, investigating their structural, magnetic, electrical, and morphological properties. The initial permeability results of $NiFe_2O_4$ and its nanocomposites revealed that these materials are good candidates for broadband transformers and communication devices. Herein, $MgFe_2O_4$ nanoparticles were synthesized via gel process, ZnO nanoparticles were prepared by co-precipitation, and the unique $(MgFe_2O_4)_{1-x}/(ZnO)_x$ nanocomposites were prepared by the solid-state method. This research may help improve the electrochemical performance of magnesium ferrite by doping with a low percentage of zinc oxide. The electrochemical performance was evaluated symmetrically using a three-electrode method in different electrolytes with the cycle voltammetry technique.

2. Preparation

2.1 Chemicals and devices required

Ferric nitrate $[Fe(NO3)3.9H2O$, 98%], and $[Mg(NO3)2.6H2O$, 98%] of magnesium nitrate, zinc chloride $[ZnCl2$, 98%], polyethylene glycol $[PEG-200$, 99%], sodium hydroxide $[NaOH$, 98%], and potassium chloride $[KC1$, 98%] were purchased from Sigma-Aldrich. All chemicals were used as received without any further purification required. LACHOI LCD Stirrer 100-2000 rpm magnetic stirrer with hot plate and timing Range 1-999 min. The Nabertherm electric furnace has a temperature range of 25-1400 °C. Pestle and mortar were made from Indian agate.

2.2 Synthesis of magnesium ferrite ($MgFe_2O_4$).

The $MgFe_2O_4$ nanoparticles were synthesized by dissolving 4 g of $Fe(NO_3)_3.9H_2O$ and 2 g of Mg $(NO_3)_2.6H_2O$ in 100 ml of ethylene glycol under constant stirring 600 rpm for 2 hours continuously at 80 °C to achieve a viscous gel. The clear solution was transferred to a hot plate and heated at 120 °C for 2 hours to facilitate thermal decomposition and eliminate volatile by-products. The residual black products were crushed by pestle and mortar, then heated at 600 °C in an electric furnace at atmospheric pressure for 3 hours to form a highly crystalline phase. Specific cation configurations and oxygen packing are necessary for the spinel structure, and greater temperatures may give atoms the energy they need to move into their proper locations.

2.3 Synthesis of zinc oxide (ZnO)

Zinc oxide nanoparticles were prepared by dissolving about 20 g of zinc chloride in 400 ml of deionized water, which was stirred at 600 rpm and 80 °C for 2 hours using a magnetic stirrer. After this, 0.5 M of NaOH solution was slowly added to the solution mentioned above, and the pH of the solution was increased up to ≈ 12. The resulting solution was then stirred for 20 min at 50 °C. The solution was then left at a typical atmospheric pressure until a white powder precipitated, and it was filtered using Whatman filter paper. Several washes with de-ionized water and ethanol were performed on the participant powder until the pH reached ≈ 7, and then it was dried at 100 °C in an oven. The dried powder was crushed by pestle and mortar, and annealed at 700 °C in an atmosphere to investigate its microstructure and electrochemical properties.

2.4 Synthesis of magnesium ferrite/zinc oxide nanocomposites

To prepare the nanocomposites, 0.09, 0.18, and 0.27 grams of magnesium ferrite nanoparticles were mixed homogeneously with 2.91, 2.82, and 2.73 grams of zinc oxide nanoparticles. Then, the mixture was ground manually using a pestle and mortar for 1 hour to achieve a highly homogeneous powder. After that, the mixed powders were sintered in an electric furnace for 4 hours at 850 °C, as shown in Fig. 1.

3. Characterization

3.1 X-ray diffraction

The crystal structure and phase purity of the prepared samples were examined using X-ray powder diffraction with a Shimadzu XD5A diffractometer, employing a $CuK\alpha$ radiation source ($\lambda = 1.5406$ Å) generated at a power setting of 40 kV and 30 mA. The diffraction data were collected in the range of 2θ ($20° < \theta < 80°$) with a scanned speed of 3°per minute and a step size of 0.04°.

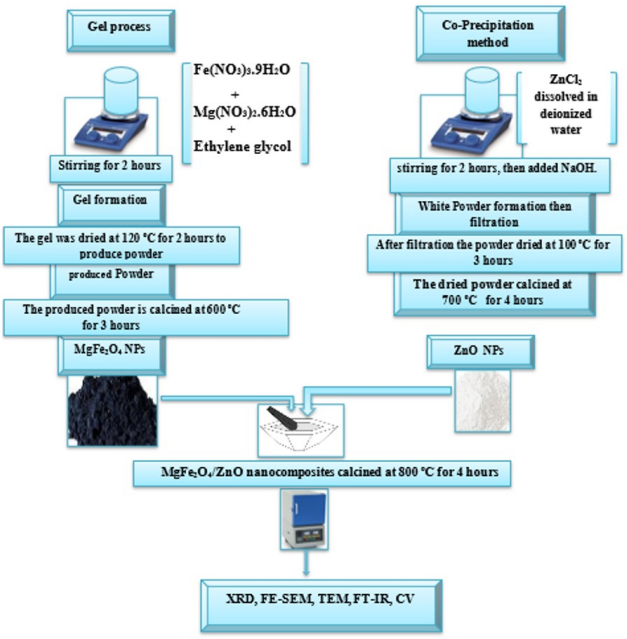

Figure 1. Schematic diagram representing the preparation of $MgFe_2O_4/ZnO$ nanocomposites.

3.2 Fourier transform infrared spectroscopy (FT-IR)

Fourier transform infrared analysis (Shimadzu, IRAffinity-1) was used to confirm the formation of the spinel structure, hexagonal wurtzite structure, and their composites. The IR spectra were recorded in the wavenumber range of 400-4000 cm^{-1}, with 10% of the prepared sample mixed with 90% potassium bromide (KBr) as a binder, and pressed under 6 tons for 3 min using a manually operated hydraulic press.

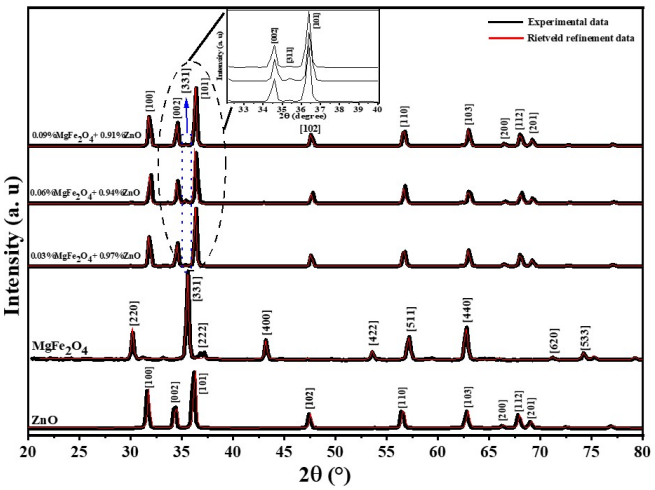

Figure 2. Rietveld refined XRD patterns were obtained for the prepared samples.

3.3 Cyclic voltammetry

The electrochemical behavior of the prepared samples was investigated using a cyclic voltammetry (CV) instrument. Cyclic voltammetry involves a three-electrode system: a platinum (Pt) wire, an $Ag/AgCl$ reference electrode, and a glassy Teflon tube, which serves as the counter, reference, and working electrodes, respectively.

3.4 Carbon paste electrode

For cycle voltammetry analysis, the working carbon paste electrodes were fabricated by carefully hand mixing (0.025 g) active materials, (0.475 g) graphite, 350 μl paraffin oil in a mortar with pestle for almost 20 min until a homogeneous sheet is produced. After standing overnight, a thin sheet was placed at the end of the teflon tube (inner diameter of 0.2 cm and outer diameter of 0.8 cm). The surface was polished using two separate techniques: first, a polishing pad and water, and subsequently, a micro-cloth disk surface and a few suspensions of alumina. The amounts of active material, modifier, and binder were chosen based on our experience and previously described articles [39]. When regeneration was necessary, the surface layer was removed and replaced with fresh paste. A copper wire was employed to make electrical contact through the center of the tube.

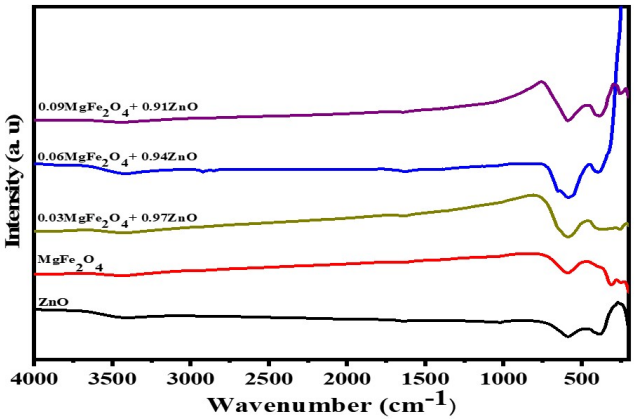

Figure 3. FT-IR spectrum of the prepared samples.

4. Results and discussion

4.1 X-ray diffraction (XRD)

The X-ray diffraction patterns of $MgFe_2O_4$ nanoparticles, ZnO nanoparticles, and $(MgFe_2O_4)_x/(ZnO)_{1-x}$ nanocomposites are presented in Fig. 2. XRD spectrum of $MgFe_2O_4$ nanoparticles in 2θ range of 20°to 80°shows diffraction peaks located at 30.2°, 35.6°, 37.22°, 43.28°, 53.7°, 57.41°, 63.02°, and 74.63°corresponding to (200), (220), (311), (222), (400), (422), (511), and (440) planes, which confirmed formation of single cubic spinel structure of $MgFe_2O_4$, respectively. All the diffraction peaks and relative intensities of $MgFe_2O_4$ are matched with the standard of JCPDS data (Card no. 73-2410). ZnO nanoparticles XRD peaks appeared at 2θ = 31.63°, 34.32°, 36.08°, 47.43°, 56.47°, 62.75°, 66.24°, 67.82°, 68.95°, and 76.84°can be ascribed to crystal planes (100), (002), (101), (102), (110), (103), (200), and (201) of zinc oxide phase. All of the reflection peaks and relative intensities are in good agreement with those of the hexagonal wurtzite phase of pure zinc oxide (ZnO) (JCPDS Card No. 01-007-2551). The results of X-ray diffraction patterns of nanocomposite samples revealed that the prepared $(MgFe_2O_4)_x/(ZnO)_{1-x}$ are heterostructures. All the diffraction peaks are consistent with JCPDS data of $MgFe_2O_4$ and ZnO nanoparticles. The high purity of the crystal structures is supported by the electron diffraction results, since there were no extra peaks or impurity phases. The crystallite size (Dxrd) and lattice parameters were estimated from the strongest peaks of XRD patterns of $MgFe_2O_4$ nanoparticles, ZnO nanoparticles, and their composites using Sherrer's equation [22, 30] as follows, Eqs. 1, 2, 3, and 4.

$$Dxrd = K\lambda/\beta\ cos\theta \tag{1}$$

$$aZnO = \sqrt{(1/3)}\ \lambda/sin\ \theta \tag{2}$$

$$C_{zno} = \lambda/sin\ \theta \tag{3}$$

$$a_{MgFe204} = d\sqrt{h^2+k^2+l^2} \tag{4}$$

Where K is the Scherrer constant, λ is the X-ray wavelength of $CuK\alpha$ radiation, β is the full width at half maximum, θ is the Bragg's angle, d is the plane distance, and hkl are Miller indices. The obtained values are shown in Fig. 2 and tabulated in Table 1. It was revealed that the variations of lattice parameters and crystalline sizes can be explained by the exchange of metal cations between the cubic spinel structure and the hexagonal wurtzite structure. The annealing process at 850 °C may provide sufficient energy for oxygen ions from nearby nanoparticles to diffuse and react. In the low magnesium ferrite content, zinc ions mostly replace iron and magnesium ions from the spinel structure since zinc ions are available for exchange in the zinc oxide phase. The spinel phase becomes non-stoichiometric as a result of this process, namely $(MgFe_2O_4)_x/(ZnO)_{1-x}$. Thus, the interfacial substitution of Zn^{2+} ions (0.74

Å: tetrahedral site and 0.88 Å: octahedral site) of wurtzite phase by Mg^{2+} ions (0.57 Å: tetrahedral site and 0.72 Å: octahedral site) and Fe^{3+} ions (0.49 Å: tetrahedral site and 0.645 Å: octahedral site) of the single cubic phase explains the observed decrease of lattice constant and crystallite size as the x-content increases [44–48]. The slight increase in lattice parameter at x = 0.09 may be due to the high molar masses of the substitute ions.

Table 1. Structural parameters of the prepared samples.

Sample	D_{XRD} nm	D_{FE-SEM} nm	D_{TEM} nm	a and c of ZnO Å	a of $MgFe_2O_4$ Å
ZnO	23	24	26	a=2.871 c= 4.974	——-
$MgFe_2O_4$	38	41	42	——-	8.344
$0.03\%MgFe_2O_4$+ 0.97%ZnO	34	38	39	a=2.842 c= 4.929	8.387
$0.06\%MgFe_2O_4$+ 0.94%ZnO	31	34	36	a=2.831 c= 4.920	8.394
$0.09\%MgFe_2O_4$+ $0.91\%ZnO$	27	31	32	a=2.853 c= 4.931	8.397

Table 2. Rietveld refinement parameters (R_p, R_{exp},R_{wp}, and G.O.F) for the prepared samples.

Sample	R_p %	R_{exp} %	R_{wp} %	G.O.F
ZnO	05.75	05.27	08.56	01.62
$MgFe_2O_4$	11.96	17.22	09.36	00.54
$0.03\%MgFe_2O_4 + 0.97\%ZnO$	08.30	05.57	13.12	02.35
$0.06\%MgFe_2O_4 + 0.94\%ZnO$	11.65	05.72	14.86	02.59
$0.09\%MgFe_2O_4 + 0.91\%ZnO$	08.52	05.78	11.19	01.93

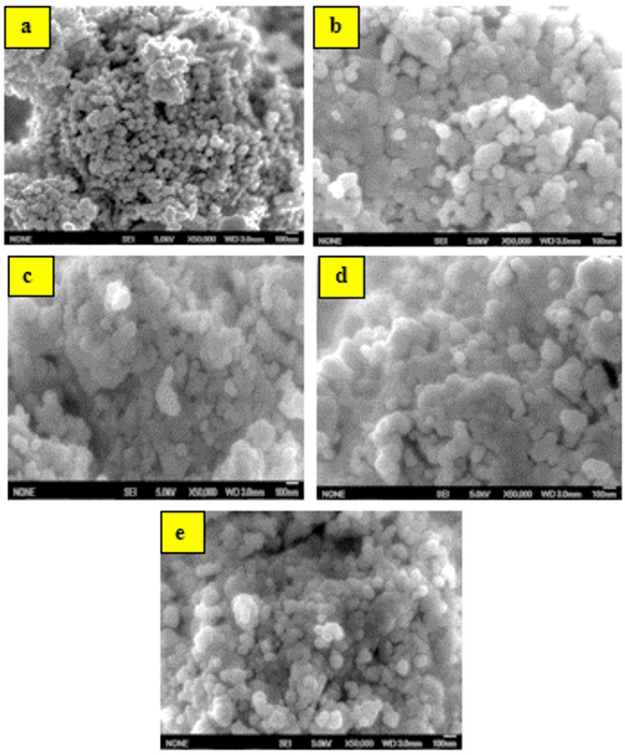

Figure 4. FE-SEM images of the prepared samples

4.2 XRD Rietveld refinements

The XRD patterns of $MgFe_2O_4$, ZnO, and their nanocomposites, Rietveld refinements using the MAUD 2.33 program, are shown in Fig. 2. The experimentally obtained XRD patterns are almost identical to the calculated XRD patterns, and so the difference between them is minimal. Experimental data and computed data are indicated by the solid black line and solid red line, respectively. The analysis structure results reveal only a single cubic and hexagonal wurtzite phase without any detectable additional peaks. The observed values of (G. O. F) justify the goodness of the refinement. Table 2 presents the structural parameters obtained from the Rietveld refinement of the fitted patterns for each sample.

4.3 Fourier transformation inferred spectroscopy (FT-IR)

Figure 3 shows Fourier transformation infrared (FT-IR) spectra of pure $MgFe_2O_4$ nanoparticles, pure ZnO nanoparticles, and $(MgFe2O4)_x/(ZnO)_{1-x}$ nanocomposites with x= 0.03, 0.06, and 0.09. The spectra exhibit a strong band at a wavenumber of 449 cm^{-1}, which corresponds to the stretching vibrations of the Zn-O bond. The formation of two fundamental metal-oxygen bands in the range of 350 cm^{-1} and 800 cm^{-1} confirms the structure of cubic spinel ferrite. The absorption band at 600 cm^{-1} is related to the nature of the stretching vibrations tetrahedral (v_1), while the absorption band at 400 cm^{-1} represents Fe-O vibrations (v_2) in octahedral (B) sites. $(MgFe2O4)_{0.03}/(ZnO)_{0.97}$ composite in Fig. 3 shows bands at 610 cm^{-1} that belong to Zn-O and at 599 cm^{-1} for Fe-O.

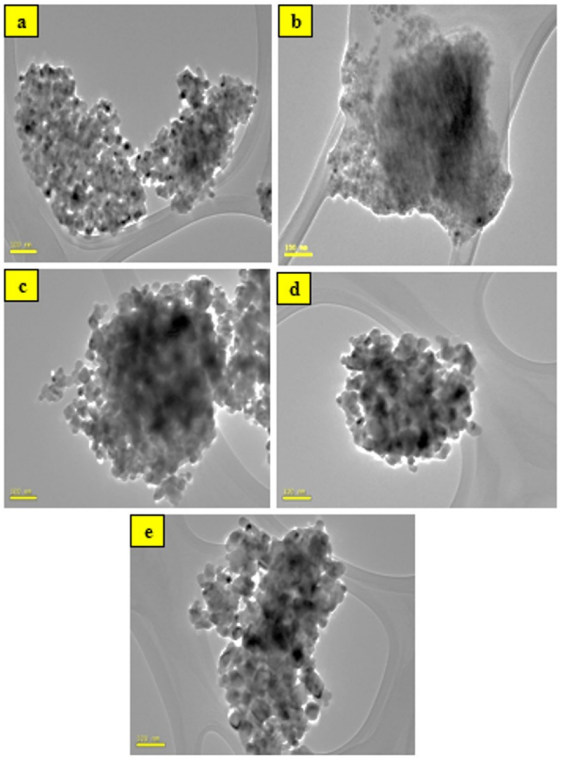

Figure 5. TEM images of the prepared samples.

4.4 Electron microscopy analysis

To gain insight into the surface morphology, all the prepared annealed samples were characterized using FE-SEM and TEM analysis. Typical FE-SEM and TEM images of the ZnO, $MgFe_2O_4$, and their composites prepared by the solid-state method with $MgFe_2O_4$ concentrations of (0.03, 0.06, and 0.09 wt%) have been shown in Fig. 4 and Fig. 5, respectively. It is observed from Fig. 4 and Fig. 5 that an almost spherical shape of the prepared samples is formed. The particle sizes of prepared samples are greater than the average crystallite size estimated from XRD's most intense peaks using the Scherrer equation. The observed variation in particle size may be caused by lattice strain and molecular structural disorder, which are induced by the clustering of nanoparticles or variations in ionic radii. The reduction in particle size with increasing Mg-ferrite content may be attributed to the mechanically induced contraction in the nanocomposite, caused by the deformation of metal-oxygen bonds. The aggregation of nanoparticles during heat treatment may be due to the net reduction between the solid-solid and solid-vapor interfaces, which

Table 3. Electrochemical parameters of CV curves in 0.5 M KC1 electrolyte.

Sample	$0.09\%MgFe_2O_4$ $+0.91\%ZnO$	$0.06\%MgFe_2O_4$ $+0.94\%ZnO$	$0.03\%MgFe_2O_4$ $+0.97\%ZnO$	$MgFe_2O_4$	ZnO
Specific capacitance (F/g) (0.01)	1.87	4.638	3.923	1.007	6.191
Energy density E (kW/kg) (0.01)	0.935	2.319	1.9615	0.5035	3.0955
Power density P (kW/kg) (0.01)	0.002337	0.00579	0.0049	0.00125	0.0773
Specific capacitance (F/g) (0.001)	6.218	6.318	5.117	7.698	6.8395
Energy density E (kW/kg) (0.001)	3.109	3.159	2.5585	3.849	3.419
Power density P (kW/kg) (0.001)	0.000777	0.000789	0.000639	0.000962	0.000854
Specific capacitance (F/g) (0.002)	4.528	5.829	7.637	8.002	14.453
Energy density E (kW/kg)(0.002)	2.264	2.9145	3.8185	4.001	7.2265
Power density P (kW/kg) (0.002)	0.001132	0.00145725	0.001909	0.002	0.007226
Specific capacitance (F/g) (0.005)	3.450	6.959	4.628	7.0514	3.732
Energy density E (kW/kg) (0.005)	1.725	3.4795	2.314	3.5257	1.866
Power density P (kW/kg) (0.005)	0.002156	0.004349	0.00289	0.004407	0.002325

Table 4. Comparison with other prepared spinel oxides.

Sample	**Synthesis method**	**Specific capacitance (F/g)**	**Electrolyte**	**Applications**	**Ref.**
$CuFe_2O_4LiB$	Chemical	02.400	1 M KOH	pseudo-capacitors	[49]
ZnO	Green synthesis	06.318	1 M NaOH	Super-capacitor	[50]
$CuFe_2O_4$	Spray pyrolysis	04.000	1 M NaOH	Super-capacitor	[51]
$MnFe_2O_4$	Thermal decomposition	10.120	0.5 M Na_2SO_4	———	[52]
$NiZnFe_2O_4$	Chemical deposition	09.000	6 M KOH	Energy storage devices	[53]
ZnO	Chemical method	14.430	0.5 M $KC1$	Pseudo-capacitors	Current study
$MgFe_2O_4$	Gel process	08.002	0.5 M $KC1$	Pseudo-capacitors	Current study

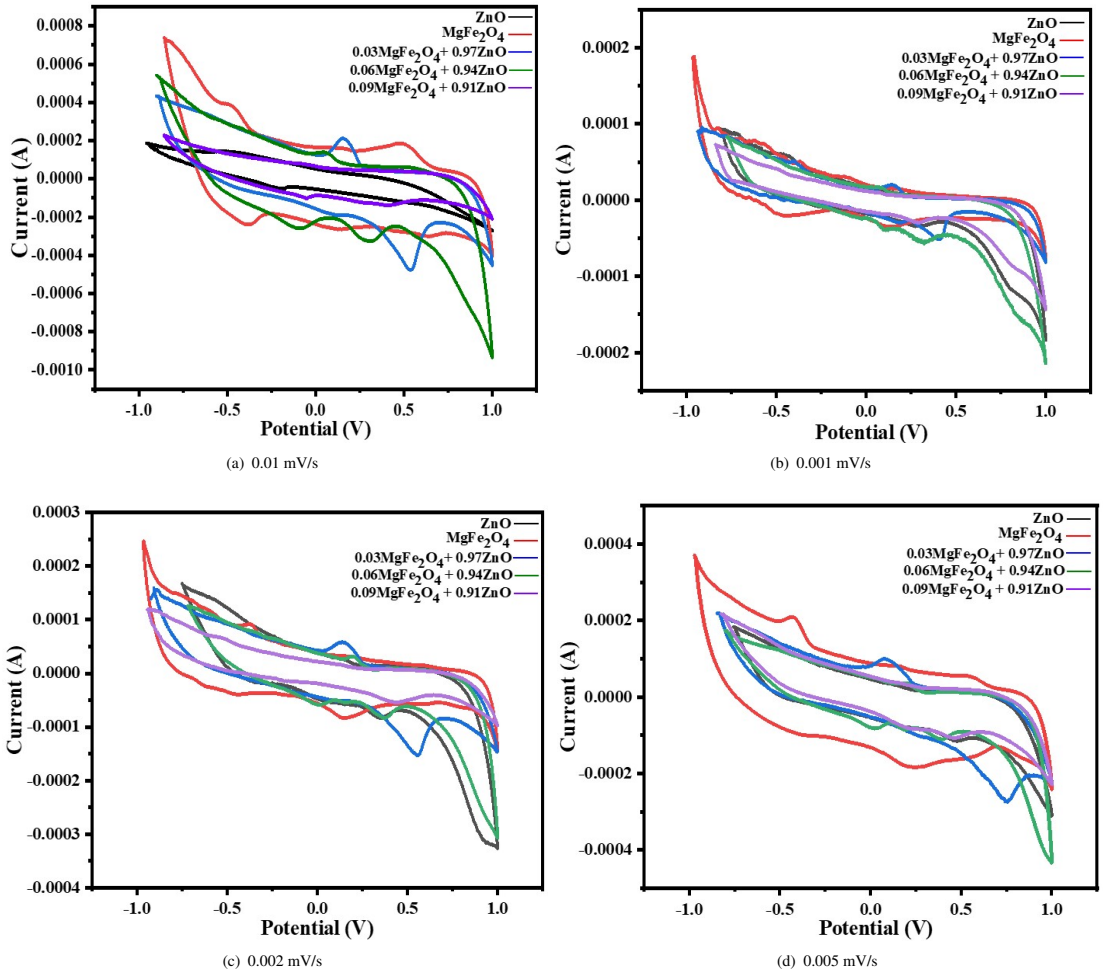

(a) 0.01 mV/s (b) 0.001 mV/s

(c) 0.002 mV/s (d) 0.005 mV/s

Figure 6. Cyclic voltameter at different scan rates.

drives grain growth during the annealing process. Furthermore, the fact that nanoparticles have a high surface area-to-volume ratio and a high level of interfacial surface tension may also contribute to particle agglomeration. The agglomeration indicates the high reactivity of the prepared samples with heat treatment, which arises from magnetic or exchange interactions between particles.

4.5 Electrochemical performance investigation

The electrochemical properties of pure and nanocomposite electrodes were investigated in a 0.5 M KC1 solution using cyclic voltammetry and charge-discharge measurements. Fig. 6a, b, c, and d indicate the cyclic voltammetry curves of pure and different ratios of $MgFe_2O_4/ZnO$ nanocomposites at which the potential window begins from -1 V to 1 V at a scan rate of 0.01, 0.001, 0.002, and 0.005 VF/s in 0.5M KC1 electrolyte. Cyclic voltammetry, a type of electrochemical analysis, provides essential information on the reduction and oxidation behavior of a substance. The CV shapes revealed that the capacitance characteristic of the prepared samples is a typical pseudo-capacitance. The pseudo-capacitance mechanism of the prepared samples may depend on the electrochemical discharge and charge reactions at the interface between the electrode and electrolyte. The discharge mechanism (cathodic process) proposed for ZnO and $MgFe_2O_4$ consists of the adsorption of K^+ onto ZnO and $MgFe_2O_4$. Table 3 presents the electrochemical parameters of the prepared samples. Zn^{2+} and Mg^{2+} are reduced to Zn^+ and Mg^+, respectively, and form adsorption complexes with K^+ to yield $ZnOK$ and $K^+Mg^+Fe_2O_4$. The charging mechanism (anodic process) of pseudo capacitance involves the desorption of K^+ from $ZnOK$ and $K^+Mg^+Fe_2O_4$, and the oxidation of Zn^+ and Mg^+ to Zn^{2+} and Mg^{2+}, respectively. It is also evident that the peaks become broader with the increase in scanning rate, implying an increase in electrode resistance. The CV curve included a pair of redox peaks resulting from the sample's redox reactions. The intercalation and deintercalation of K^+ from the electrolyte into the samples primarily control the redox process [54, 55]. On the other hand, at a high scan rate, the diffusion of electrolyte ions occurs only at the outer surfaces because there is insufficient time for them to enter the material, resulting in a decrease in specific capacitance. Table 4 presents a comparison of the current results with those from the literature survey.

5. Conclusion

The structure and electrochemical properties of the $(MgFe_2O_4)_x/ZnO_{1-x}$ nanocomposites synthesized by the solid-state method were examined by XRD, FT-IR, FE-SEM, TEM, and CV. Results of XRD analysis using the Rietveld refinement model confirm the formation of single cubic spinel, hexagonal wurtzite, and composite structures. The variation in lattice constants of the above phases may be due to the exchange of ions between magnesium ferrite and zinc oxide. FT-IR spectra confirmed the formation of functional groups in the prepared samples, as evidenced by their characteristic peaks. FE-SEM images revealed some agglomerations resulting from the annealing process, which increased with the $MgFe_2O_4$ content. TEM images appeared in almost a spherical shape with a fine particle size distribution. The electrochemical behaviour of the prepared samples was investigated using cyclic voltammetry in a $KC1$ solution at various scan rates. The highest specific capacitance value found for ZnO is 14.453 F/g at a scan rate of 0.002 V. The electrochemical properties suggested that the prepared materials are a good candidate for pseudo-capacitance applications.

Authors' contribution

All authors contributed equally to the preparation of this article and approved the final version of the manuscript.

Declaration of competing interest

The authors declare no conflicts of interest.

Funding source

This study didn't receive any specific funds.

Data availability

The data that support the findings of this study are available from the corresponding author upon reasonable request.

Acknowledgements

The authors would like to acknowledge Universiti Teknologi Malaysia (UTM) for TEM characterizations.

REFERENCES

[1] Y. Verma, V. Mishra, L. Agarwal, L. Singh, and S. Gupta, "Study of different transport properties of mgzno/zno and algan/gan high electron mobility transistors: A review," *HEMT Technology and Applications.Springer Tracts in Electrical and Electronics Engineering. Springer*, pp. 53–69, 2023. [Online]. Available: https://doi.org/10.1007/978-981-19-2165-0_4

[2] S. Sulaiman, N. Zamri, R. Aziz, M. Sharif, N. Nawawi, and N. Jamal, "Effects of solvents on zno nanoparticles synthesis via sol–gel method," *Technological Advancement in Mechanical and Automotive Engineering*, pp. 181–189, 2023. [Online]. Available: https://doi.org/10.1007/978-981-19-1457-7_14

[3] Z. Wang, "Nanostructures of zinc oxide," *Materials Today*, vol. 7, no. 6, pp. 26–33, 2004. [Online]. Available: https://doi.org/10.1016/S1369-7021(04)00286-X

[4] L. Schlur, J. Calado, and D. Spitzer, "Synthesis of zinc oxide nanorods or nanotubes on one side of a microcantilever," *Royal Society open science*, vol. 5, no. 8, p. 180510, 2018. [Online]. Available: https://doi.org/10.1098/rsos.180510

[5] H. Greijer, N. Mirotta, E. Treossi, F. Valorosi, F. Schütt, L. Siebert, Y. Mishra, R. Adelung, V. Palermo, and H. Hillborg, "Tuneable conductivity at extreme electric fields in zno tetrapod-silicone composites for high-voltage power cable insulation," *Scientific Reports*, vol. 12, p. 6035, 2022. [Online]. Available: https://doi.org/10.1038/s41598-022-09966-4

[6] H. Savaloni and R. Savari, "Nano-structural variations of zno:n thin films as a function of deposition angle and annealing conditions: Xrd, afm,fesem and eds analyses," *Materials Chemistry and Physics*, vol. 214, pp. 402–420, 2018. [Online]. Available: https://doi.org/10.1016/j.matchemphys.2018.04.099

[7] A. Phuruangrat, A. Nunpradit, T. Sakhon, P. Dumrongrojthanath, N. Ekthammathat, S. Thongtem, and T. Thongtem, "Microwave-assisted synthesis of heterostructure pd/zno flowers used for photocatalytic reaction of dyes illuminated by uv radiation," *Journal of the Australian Ceramic Society*, vol. 57, pp. 1521–1530, 2021. [Online]. Available: https://doi.org/10.1007/s41779-021-00642-w

[8] R. Jing, A. I. Khursheed, J. Song, L. Sun, Z. Yu, Z. Nie, and E. Cao, "A comparative study on the acetone sensing properties of zno disk pairs, flowers, and walnuts prepared by hydrothermal method," *Applied Surface Science*, vol. 591, p. 153218, 2022. [Online]. Available: https://doi.org/10.1016/j.apsusc.2022.153218

[9] X. Pan, J. Zhang, H. Zhou, R. Liu, D. Wu, R. Wang, L. Shen, L. Tao, J. Zhang, and H. Wang, "Single-layer zno hollow hemispheres enable high-performance self-powered perovskite photodetector for optical communication," *Nano-Micro Letters*, vol. 13, no. 70, pp. 1–12, 2021. [Online]. Available: https://doi.org/10.1007/s40820-021-00596-5

[10] L. Li, V. Senina, G. Goryunov, and D. Kostomarov, "Zno@si(100) and zno@si(111): Hydrothermal synthesis, morphology, and lasing characteristics," *Crystallography Reports*, vol. 64, pp. 419–421, 2019. [Online]. Available: https://doi.org/10.1134/S1063774519020196

[11] A. Hssaini, M. Belaiche, M. Elansary, C. Ferdi, and Y. Mouhib, "Magnetic and structural properties of novel-coated ni0.5co0.5fe1.6gd0.2mo0.1sm0.1o4 spinel ferrite nanomaterial: Experimental and theoretical investigations," *Journal of Superconductivity and Novel Magnetism*, vol. 35, no. 2016, pp. 2799–2820, 2022. [Online]. Available: https://doi.org/10.1007/s10948-022-06307-4

[12] S. Alardhi, A. Abdalsalam, A. Ati, M. Abdulkareem, A. Ramadhan, M. Taki, and Z. Abbas, "Fabrication of polyaniline/zinc oxide nanocomposites: synthesis, characterization and adsorption of methylene orange," *Polymer Bulletin*, vol. 81, pp. 1131–1157, 2024. [Online]. Available: https://doi.org/10.1007/s00289-023-04753-1

[13] S. Parui, V. Kheraj, N. Tiwari, and R. Chauhan, "Development of ni-doped zinc oxide films via sol-gel synthesis," *Micro and Nanoelectronics Devices, Circuits and Systems*, vol. 904, pp. 3–9, 2023. [Online]. Available: https://doi.org/10.1007/978-981-19-2308-1_1

[14] A. Ati, A. Abdalsalam, and H. Abbas, "Influence of annealing on structural, morphology, magnetic and optical properties of pld deposited cufe2o4 thin films," *Inorganic Chemistry Communications*, vol. 146, p. 110072, 2022. [Online]. Available: https://doi.org/10.1016/j.inoche.2022.110072

[15] R. Khalil, M. Azar, I. Malham, M. Turmine, and V. Vivier, "Electrochemical deposition of zno thin films in aprotic ionic liquids: Effect of the cationic alkyl-chain-length," *Journal of Ionic Liquids*, vol. 2, no. 1, p. 100031, 2022. [Online]. Available: http://doi.org/10.1016/j.jil.2022.100031

[16] P. Shankar, P. Srinivasan, B. Vutukuri, A. Kulandaisamy, G. Mani, K. Babu, J. Lee, and J. Rayappan, "Boron induced c-axis growth and ammonia sensing signatures of spray pyrolysis deposited zno thin films – relation

between crystallinity and sensing," *Thin Solid Films*, vol. 746, p. 139126, 2022. [Online]. Available: https://doi.org/10.1016/j.tsf.2022.139126

[17] H. V. Han, D. Du, and D. Tuan, "Comparing the application of gas sensor fabrication of nanomaterials zno fabricated by hydrothermal and chemical vapor deposition method," *Advances in Engineering Research and Application*, vol. 178, pp. 254–261, 2021. [Online]. Available: https://doi.org/10.1007/978-3-030-64719-3_29

[18] S. Rahmane and M. Djouadi, "Optoelectronic properties of zno thin films grown by radio frequency magnetron sputtering," *Journal of Materials Science: Materials in Electronics*, vol. 31, pp. 17 872–17 878, 2020. [Online]. Available: https://doi.org/10.1007/s10854-020-04340-4

[19] I. R. Foumani and S. Pat, "Optical and surface properties of gd-doped zno thin films deposited by thermionic vacuum arc deposition technology," *Inorganic Chemistry Communications*, vol. 144, p. 109831, 2022. [Online]. Available: https://doi.org/10.1016/j.inoche.2022.109831

[20] G. Saravanavel, S. Honnali, K. Lourdes, S. John, and K. Gunasekhar, "Study on the thermoelectric properties of al-zno thin-film stack fabricated by physical vapour deposition process for temperature sensing," *Sensors and Actuators A: Physical*, vol. 332, no. part 1, p. 113097, 2021. [Online]. Available: https://doi.org/10.1016/j.sna.2021.113097

[21] F.-X. Jiang, G.-Z. Zhang, L.-F. Ji, L.-M. Zhao, and X.-H. Xu, "Effect of cr, n co-doping on the structural and optical properties of zno thin films deposited by pulsed laser deposition," *Journal of Materials Science: Materials in Electronics*, vol. 33, pp. 12 408–12 415, 2022. [Online]. Available: https://doi.org/10.1007/s10854-022-08198-6

[22] A. Abdalsalam, A. Ati, A. Abduljabbar, and T. Hussein, "Structural, optical, electrical and magnetic studies of pani/ferrite nanocomposites synthesized by pld technique," *Journal of Inorganic and Organometallic Polymers and Materials*, vol. 29, pp. 1084–1093, 2019. [Online]. Available: https://doi.org/10.1007/s10904-018-0997-2

[23] M. El-Shaarawy, M. Khairy, and M. Mousa, "Structural, electrical and electrochemical properties of zno nanoparticles synthesized using dry and wet chemical methods," *Advanced Powder Technology*, vol. 31, no. 3, pp. 1333–1341, 2020. [Online]. Available: https://doi.org/10.1016/j.apt.2020.01.009

[24] X. He, J. E. Yoo, M. H. Lee, and J. Bae, "Morphology engineering of zno nanostructures for high performance supercapacitors: enhanced electrochemistry of zno nanocones compared to zno nanowires," *Nanotechnology*, vol. 28, no. 24, p. 245402, may 2017. [Online]. Available: https://doi.org/10.1088/1361-6528/aa6bca

[25] M. H. Khashan and A. K. Mohammad, "Comparative study for pb2+ adsorption from simulated wastewater of battery manufacture on activated carbon prepared from rice husk with different activation agents," *Al-Qadisiyah Journal for Engineering Sciences*, vol. 15, no. 3, pp. 147–155, 2022. [Online]. Available: https://doi.org/10.30772/qjes.v15i3.827

[26] F. T. Aula, "Voltage equalizer enhancement of series-connected battery strings using variable duty cycle pwm of a dynamic capacitor circuit," *Qadisiyah Journal for Engineering Sciences*, vol. 18, no. 2, p. 190 – 196, 2025. [Online]. Available: https://doi.org/10.30772/qjes.2024.146300.1100

[27] N. Kher, K. Boora, K. Yadav, and V. Kumar, "Harnessing solar energy: Hardware implementation of solar power inverter," *Qadisiyah Journal for Engineering Sciences*, vol. 18, no. 2, p. 221 – 232, 2025. [Online]. Available: https://doi.org/10.30772/qjes.2024.152932.1367

[28] W. J. K. Al-Obaidi and W. Jamshed, "A numerical study of the effects of various diesel fuel types on the performance of single-cylinder diesel engines," *Qadisiyah Journal for Engineering Sciences*, vol. 17, no. 4, p. 436–444, 2024. [Online]. Available: https://doi.org/10.30772/qjes.2024.153932.1401

[29] P. Y. Andoha, C. K. K. Sekyere, K. O. Amoabenga, and D. E. K. Dzebrea, "Performance assessment of a solar powered egg incubator with a backup heater," *Al-Qadisiyah Journal for Engineering Sciences*, vol. 15, no. 2, pp. 112–120, 2022. [Online]. Available: https://doi.org/10.30772/qjes.v15i2.821

[30] R. Godbole, P. Rao, P. Alegaonkar, and S. Bhagwat, "Influence of fuel to oxidizer ratio on lpg sensing performance of mgfe2o4 nanoparticles," *Materials Chemistry and Physics*, vol. 161, pp. 135–141, 2015. [Online]. Available: https://doi.org/10.1016/j.matchemphys.2015.05.028

[31] R. S. Priya, E. R. Kumar, A. Balamurugan, and C. Srinivas, "Green synthesized mgfe2o4 ferrites nanoparticles for biomedical applications," *Applied Physics A*, vol. 127, no. 538, 2021. [Online]. Available: https://doi.org/10.1007/s00339-021-04699-z

[32] R. S. Priya, P. Chaudhary, E. R. Kumar, A. Balamurugan, C. Srinivas, G. Prasad, B. Yadav, and D. Sastry, "Evaluation of structural, dielectric and electrical humidity sensor behaviour of mgfe2o4 ferrite nanoparticles," *Ceramics International*, vol. 47, no. 11, pp. 15 995–16 008, 2021. [Online]. Available: https://doi.org/10.1016/j.ceramint.2021.02.174

[33] F. Alshorifi, S. Ali, and R. Salama, "Promotional synergistic effect of cs–au nps on the performance of cs–au/mgfe2o4 catalysts in catalysis 3,4-dihydropyrimidin-2(1h)-ones and degradation of rhb dye," *Journal of Inorganic and Organometallic Polymers and Materials, 32 (2022)* ., vol. 32, p. 3765–3776, 2022. [Online]. Available: https://doi.org/10.1007/s10904-022-02389-8

[34] J. Wang, A. Sun, Y. Jiang, X. Huang, L. Shao, and Y. Zhang, "Structural and magnetic properties of ce3+doped mg-co ferrite prepared by sol–gel method," *Journal of Materials Science: Materials in Electronics*, vol. 33, pp. 11 881–11 895, 2022. [Online]. Available: https://doi.org/10.1007/s10854-022-08150-8

[35] A. Ati, A. Abdalsalam, and A. Hasan, "Thermal, microstructural and magnetic properties of manganese substitution cobalt ferrite prepared via co-precipitation method," *Journal of Materials Science: Materials in Electronics*, vol. 32, pp. 3019–3037, 2021. [Online]. Available: https://doi.org/10.1007/s10854-020-05053-4

[36] A. Ati, "Fast synthesis, structural, morphology with enhanced magnetic properties of cobalt doped nickel ferrite nanoscalerg," *Journal of Materials Science: Materials in Electronics*, vol. 29, pp. 12 010–12 021, 2018. [Online]. Available: https://doi.org/10.1007/s10854-018-9305-8

[37] J. Gonçalves, L. de Faria, A. Nascimento, R. Germscheidt, S. Patra, L. Hernández-Saravia, J. Bonacin, R. Munoz, and L.Angnes, "Sensing performances of spinel ferrites mfe2o4 (m = mg, ni, co, mn, cu and zn) based electrochemical sensors: A review," *Analytica Chimica Acta*, vol. 1233, p. 340362, 2022. [Online]. Available: https://doi.org/10.1016/j.aca.2022.340362

[38] U. Wongpratat, P. Tipsawat, J. Khajonrit, E. Swatsitang, and S. Maensiri, "Effects of nickel and magnesium on electrochemical performances of partial substitution in spinel ferrite," *Journal of Alloys and Compounds*, vol. 831, p. 154718, 2020. [Online]. Available: https://doi.org/10.1016/j.jallcom.2020.154718

[39] Z. Heiba, M. Sanad, and M. Mohamed, "Influence of mg-deficiency on the functional properties of magnesium ferrite anode material," *Solid State Ionics*, vol. 341, p. 115042, 2019. [Online]. Available: https://doi.org/10.1016/j.ssi.2019.115042

[40] Y. Li, T. Wang, S. Zhang, Y. Zhang, L. Yu, and R. Liu, "Adsorption and electrochemical behavior investigation of methyl blue onto magnetic nickel-magnesium ferrites prepared via the rapid combustion process," *Journal of Alloys and Compounds*, vol. 885, p. 160969, 2021. [Online]. Available: https://doi.org/10.1016/j.jallcom.2021.160969

[41] B. Janani, S. Al-amri, M. Okla, A. Mohebaldin, W. Soufan, B. Almunqedhi, M. Abdel-Maksoud, H. AbdElgawad, A. Thomas, L.L.Raju, and S. Khan, "High performing p-n system of cafe2o4 coupled zno for synergetic degradation of rhodamine b with white-light photocatalysis and bactericidal action," *Journal of the Taiwan Institute of Chemical Engineers*, vol. 133, p. 104271, 2022. [Online]. Available: https://doi.org/10.1016/j.jtice.2022.104271

[42] S. Munir, M. F. Warsi, S. Zulfiqar, I. Ayman, S. Haider, I. Alsafari, P. Agboola, and I. Shakir, "Nickel ferrite/zinc oxide nanocomposite: Investigating the photocatalytic and antibacterial properties," *Journal of Saudi Chemical Society,*, vol. 25, no. 12, p. 101388, 2021. [Online]. Available: https://doi.org/10.1016/j.jscs.2021.101388

[43] A. Hamed, I. Ali, M. E. Ghazaly, and H. H. M. Al-Abyad, "Nanocomposites of zno mixed with different ni-ferrite contents: Structural and magnetic properties," *Physica B: Condensed Matter*, vol. 607, p. 412861, 2021. [Online]. Available: https://doi.org/10.1016/j.physb.2021.412861

[44] K. Schachl, H. Alemu, K. Kalcher, J. Ježkova, I. Švancara, and K. Vytřas, "Amperometric determination of hydrogen peroxide with a manganese dioxide-modified carbon paste electrode using flow injection analysis," *Analyst*, vol. 122, pp. 985–989, 1997. [Online]. Available: https://doi.org/10.1039/A701723E

[45] E. O'Quinn, J. Shamblin, B. Perlov, R. Ewing, J. Neuefeind, M. Feygenson, I. Gussev, and M. Lang, "Inversion in mg1–xnixal2o4 spinel: New insight into local structure," *Journal of the American Chemical Society*, vol. 139, no. 30, pp. 10 395–10 402, 2017. [Online]. Available: https://doi.org/10.1021/jacs.7b04370

[46] T. Dippong, E. Levei, I. Deac, and O. C. E. Neag, "Influence of cu2+, ni2+, and zn2+ ions doping on the structure, morphology, and magnetic properties of co-ferrite embedded in sio2 matrix obtained by an innovative sol-gel route," *Nanomaterials*, vol. 10, no. 3, p. 580, 2020. [Online]. Available: https://doi.org/10.3390/nano10030580

[47] C. Liu, Z. Neale, J. Zheng, X. Jia, M. Y. J. Huang, M. Tian, M. Wang, J. Yang, and G. Cao, "Expanded hydrated vanadate for high-performance aqueous zinc-ion batteries," *Energy Environmental Science*, vol. 12, no. 7, pp. 2273–2285, 2019. [Online]. Available: https://doi.org/10.1039/C9EE00956F

[48] H. Wu, Q. Zhu, X. Sun, and J.-G. Li, "Regulating anti-site defects in mgga2o4:mn4+ through mg2+/ge4+ doping to greatly enhance broadband red emission for plant cultivation," *Journal of Materials Research and Technology*, vol. 13, pp. 1–12, 2021. [Online]. Available: https://doi.org/10.1016/j.jmrt.2021.04.045

[49] A. Rocha, L. Magnago, J. Santos, V. Leal, A. Marins, V. Pegoretti, S. Ferreira, M. Lelis, and M. Freitas, "Copper ferrite synthesis from spent li-ion batteries for multifunctional application as catalyst in photo fenton process and as electrochemical pseudocapacitor," *Materials Research Bulletin*, vol. 113, pp. 231–240, 2019. [Online]. Available: https://doi.org/10.1016/j.materresbull.2019.02.007

[50] S. Yadav, N. Rani, and K. Saini, "Green synthesis of zno and cuo nps using ficus benghalensis leaf extract and their comparative study for electrode materials for high performance supercapacitor application," *Materials Today: Proceedings*, vol. 49, no. Part 5, pp. 2124–2130, 2022. [Online]. Available: https://doi.org/10.1016/j.matpr.2021.08.323

[51] D. Ham, J. Chang, S. Pathan, W. Kim, R. Mane, B. Pawar, O.-S. Joo, H. Chung, M.-Y. Yoon, and S.-H. Han, "Electrochemical capacitive properties of spray-pyrolyzed copper-ferrite thin films," *Current Applied Physics.*, vol. 9, no. 1, pp. S98–S100, 2009. [Online]. Available: https://doi.org/10.1016/j.cap.2008.08.042

[52] G. Singh and S. Chandra, "Electrochemical performance of mnfe2o4 nano-ferrites synthesized using thermal decomposition method," *international journal of hydrogen energy*, vol. 43, no. 8, pp. 4058–4066, 2018. [Online]. Available: https://doi.org/10.1016/j.ijhydene.2017.08.181

[53] D. Pawar, J. Shaikh, B. Pawar, S. Pawar, P. Patil, and S. Kolekar, "Synthesis of hydrophilic nickel zinc ferrite thin films by chemical route for supercapacitor application," *Journal of Porous Materials*, vol. 19, pp. 649–655, 2012. [Online]. Available: https://doi.org/10.1007/s10934-011-9516-3

[54] R. Wang, Q. Li, L. Cheng, H. Li, B. Wang, X. Zhao, and P. Guo, "Electrochemical properties of manganese ferrite-based supercapacitors in aqueous electrolyte: The effect of ionic radius," *Colloids and Surfaces A: Physicochemical and Engineering Aspects*, vol. 457, pp. 94–99, 2014. [Online]. Available: https://doi.org/10.1016/j.colsurfa.2014.05.059

[55] G. Singh and S. Chandra, "Nano-flowered manganese doped ferrite@pani composite as energy storage electrode material for supercapacitors," *Journal of Electroanalytical Chemistry*, vol. 874, p. 114491, 2020. [Online]. Available: https://doi.org/10.1016/j.jelechem.2020.114491

How to cite this article:
Alyaa H. Abdalsalam, Noor Malik Saadon, Ali A. Ati, S Dabagh, and AA Salim (2025). 'Investigation of the structural, morphological, and electrochemical characteristics of $MgFe_2O_4/ZnO$ nanocomposite', Al-Qadisiyah Journal for Engineering Sciences, 18 (4), pp. 352-359. https://doi.org/10.30772/qjes.2025.160113.1559